Front. Mech. Eng. 2024, 19(4): 28
https://doi.org/10.1007/s11465-024-0800-8

RESEARCH ARTICLE

Force model in electrostatic atomization minimum quantity lubrication milling GH4169 and performance evaluation

Min YANG[a,b], Hao MA[a], Zhonghao LI[a], Jiachao HAO[a], Mingzheng LIU[a], Xin CUI[a], Yanbin ZHANG[a], Zongming ZHOU[c], Yunze LONG[b], Changhe LI (✉)[a]

[a] *School of Mechanical and Automotive Engineering, Qingdao University of Technology, Qingdao 266520, China*
[b] *College of Physics, Qingdao University, Qingdao 266071, China*
[c] *Hanergy Lubrication Technology Co., Ltd., Qingdao 266200, China*

✉ *Corresponding author. Email: sy_lichanghe@163.com (Changhe LI)*

© Higher Education Press 2024

ABSTRACT The nickel-based high-temperature alloy GH4169 is the material of choice for manufacturing critical components in aeroengines, and electrostatic atomization minimum quantity lubrication (EMQL) milling represents a fundamental machining process for GH4169. However, the effects of electric field parameters, jet parameters, nozzle position, and milling parameters on milling performance remain unclear, which constrains the broad application of EMQL in aerospace manufacturing. This study evaluated the milling performance of EMQL on nickel-based alloys using soybean oil as the lubrication medium. Results revealed that compared with conventional pneumatic atomization MQL milling, EMQL reduced the milling force by 15.2%–15.9%, lowered the surface roughness by 30.9%–54.2%, decreased the average roughness spacing by 47.4%–58.3%, and decreased the coefficient of friction and the specific energy of cutting by 55% and 19.6%, respectively. Subsequent optimization experiments using orthogonal arrays demonstrated that air pressure most significantly affected the milling force and specific energy of cutting, with a contribution rate of 22%, whereas voltage had the greatest effect on workpiece surface roughness, contributing 36.71%. Considering the workpiece surface morphology and the potential impact of droplet drift on environmental and health safety, the optimal parameter combination identified were a flow rate of 80 mL/h, an air pressure of 0.1 MPa, a voltage of 30 kV, a nozzle incidence angle of 35°, an elevation angle of 30°, and a target distance of 40 mm. This research aimed to provide technical insights for improving the surface integrity of aerospace materials that are difficult to machine during cutting operations.

KEYWORDS electrostatic atomization, MQL, nickel-based alloys, milling force, surface roughness, force model

1 Introduction

The nickel-based high-temperature alloy GH4169 is widely utilized in the manufacturing of aeroengine parts, particularly turbine disks, because of its exceptional properties, such as high-temperature strength, high hardness, oxidation resistance, and corrosion resistance. One common and fundamental machining process in the production of GH4169 parts is milling. However, despite its favorable mechanical properties, GH4169 presents challenges in machining, such as milling difficulty, high milling temperature, and high residual stress [1–3]. When milling nickel-based alloys, the force and heat interactions between the cutting areas are significant. A high-flow cutting fluid supply mode is typically employed to ensure adequate cooling and lubrication during the cutting process [4–6]. Unfortunately, this approach introduces problems such as environmental pollution and low cutting fluid utilization [7]. Researchers have proposed an alternative method called minimum quantity lubrication (MQL) [8,9], which aims to minimize the amount of lubricant and provide cooling and lubrication in the cutting zone. In this method, a microlubricant is mixed with compressed air inside a two-phase flow nozzle and atomized into a fine-particle oil mist. The mist is then transported to the cutting zone by the air jet and forms an oil film, providing the necessary cooling and lubricating effect. Although the microlubrication method reduces the supply of lubricant, it still faces certain technical challenges. Microlubricants rely on high-pressure gas atomization, making it difficult to control the droplet size, distribution, and transport accuracy during

Received March 8, 2024; accepted April 26, 2024; online August 20, 2024

air field perturbation. Moreover, the generated droplets, including PM10 and PM2.5, can be inhaled and pose a threat to the effective utilization of the cutting fluid and the environment, as well as the health of the staff. Therefore, there is a pressing need to find a new type of atomization method that can produce fine particles of oil, improve penetration and deposition performance, and prevent the drift of small droplets [10].

Electrostatic atomization technology has demonstrated remarkable advantages in various high-tech fields, such as the preparation of raw nanoparticles, nanocapsules, nanofibers, and fuel cells [11–13]. It is characterized by a small atomized particle size, high homogeneity, and strong encapsulation. Furthermore, studies on coal–water slurry atomization, liquid fuel atomization, and electrostatic spraying have demonstrated that charge atomization can enhance droplet particle size refinement, reduce droplet size distribution, and improve the effective deposition rate and uniformity [14–16]. Consequently, the use of electrostatic atomization minimum quantity lubrication (EMQL) technology in GH4169 milling processing is anticipated to provide precise and controllable cutting fluid droplet size distribution and transport [17]. Moreover, it can enhance the effective utilization of cutting fluid while safeguarding the environment and promoting staff health.

In recent years, extensive research has been conducted on milling processes using EMQL. Huang et al. [18] investigated the effect of EMQL on stainless steel vertical milling by comparing dry, flood cooling, and MQL techniques. They conducted EMQL stainless steel milling tests and found that compared with traditional flood and MQL machining methods, EMQL significantly reduces tool wear and cutting force while extending tool life and enhancing surface finish. Similarly, Xu et al. [19] studied the process parameters for the vertical milling of AISI-304 stainless steel using EMQL and compared them with those of dry, flood, and MQL machining. They conducted parameter tests under EMQL conditions and concluded that voltage and air pressure are the critical parameters for EMQL. A low air pressure (0.4 MPa) is effective at improving tool life, reducing grinding force, and achieving remarkable surface roughness. Huang et al. [20] analyzed the process parameters of AISI-304 stainless steel EMQL milling and compared the wetting and penetration of LB-2000 vegetable oil under different electrostatic voltages. Their results showed that LB-2000 vegetable oil exhibits superior wetting and penetration ability under EMQL conditions. A reduced droplet diameter allows for effective lubricating oxygen mist to enter the contact interface. Another study by Huang et al. [21] investigated the turning performance of EMQL on AISI 304 stainless steel. They compared the tool wear, cutting force, and surface quality of electrostatic atomized trace lubrication, full dry cutting, conventional flood cutting, and MQL under different cutting conditions. Their results demonstrated that EMQL offers better lubrication, reducing tool wear, and cutting force, thereby achieving higher surface quality compared with the other methods. Additionally, Xu et al. [8] examined the milling performance of Al_2O_3 water-based nanofluid EMQL. They compared the capillary penetration mechanism, oil mist concentration, and heat transfer performance of Al_2O_3 fluid EMQL and MQL. Researchers have conducted EMQL stainless steel milling experiments and found that EMQL effectively improves lubricating oil penetration and heat transfer. Compared with Al_2O_3 fluid MQL and oil-based MQL, Al_2O_3 water-based nanofluid EMQL significantly reduces the oil mist concentration, cutting temperature, friction, and tool wear, ultimately enhancing machining performance. Lv et al. [22] investigated the milling performance of SiO_2 water-based nanofluid EMQL by assessing its performance at different voltages. They found that SiO_2 water-based nanofluids exhibit better chargeability than vegetable oil, resulting in superior penetration, adsorption, and deposition. De Bartolomeis et al. [23] proposed a novel design scheme for EMQL nozzles to explore the milling performance of Inconel 718 high-temperature alloys. They compared tool life, cutting specific energy, and surface roughness under EMQL and MQL conditions. Researchers have conducted vertical milling tests on Inconel 718 under EMQL conditions and observed that EMQL machining provides better surface quality and improved tool life compared with conventional MQL. Furthermore, Xu et al. [24] investigated the machinability of AlSi7Mg alloys in high-speed milling using EMQL. They performed parametric tests under EMQL conditions, comparing them with dry, cast, and conventional MQL conditions. Their results indicated that compared with dry, cast, and conventional MQL methods, EMQL offers superior lubrication and cooling effects in the high-speed cutting of AlSi7Mg alloys, yielding the best surface quality, minimum tool wear, and adhesion. Finally, Liu et al. [25] analyzed the milling performance of Ti–6Al–4V titanium alloy using cold air EMQL. They compared the cutting force, cutting temperature, surface roughness, tool life, tool wear, and chip morphology under different cooling methods. Their experiments revealed that cold air EMQL improves the critical heat flux density and steady-state heat transfer performance. This results in a low milling force, reduced milling temperature, improved surface quality, and decreased tool wear.

In summary, the use of EMQL technology to improve milling performance plays a significant role in this improvement. However, current research primarily focuses on studying the impact of specific conditions, such as air pressure, voltage, and atomization parameters, on machining performance. Factors such as workpiece material characteristics, the relative position of the nozzle and cutting zone, and changes in milling parameters and characteristics can affect the milling force. Currently,

there is a lack of research on optimizing EMQL process parameters through the adjustment of spatial field parameters, as well as a lack of corresponding data support. To address this gap, we designed evaluation and optimization experiments for the EMQL milling of nickel-based alloys. This study considered field parameters, positional parameters (flow rate, air pressure, voltage, angle of incidence, elevation angle, and target distance), and other factors that influence milling force, cutting specific energy, and surface roughness. The aim was to identify the best process parameters for optimal EMQL applications and provide technical support for improving the surface integrity of difficult-to-machine materials.

2 Force model and milling performance evaluation parameters

The force experienced by the cutting edge when in contact with the machined part is caused by the elastic deformation of the material in the cutting zone. Without considering material deformations, nonlinear properties, or microscopic changes, the cutting force can be solved by separating the cutting edge into microelements. Each microelement can be treated as an oblique cutting process, and the cutting force can be solved using an analytical model for oblique cutting. The cutting parameters are determined based on the geometric relationship between the cutter and workpiece movement, and the total cutting force is obtained by integrating along the axial direction and the number of teeth.

2.1 Milling force model

For example, when using an end milling cutter to mill a workpiece, the axial cutting thickness is denoted as α_e. The center of the milling cutter endface circle is taken as the coordinate origin, and a 3D model of the milling force is established (Fig. 1). The helical edge of the milling cutter is discretized into a certain number of small units dz, which are evenly spaced along the axial direction [26–28]. The cutting motion of each microelement of the cutting edge at any given moment can be considered an independent bevel cutting process [17,29−31]. The radial, tangential, and axial forces on the cutting edge microcells at the axial height z of the milling cutter are given by Eq. (1).

$$\begin{cases} \mathrm{d}F_{\mathrm{t}}(\varphi,z) = K_{\mathrm{tc}}h[\varphi(z)]\mathrm{d}z + K_{\mathrm{te}}\mathrm{d}z, \\ \mathrm{d}F_{\mathrm{r}}(\varphi,z) = K_{\mathrm{rc}}h[\varphi(z)]\mathrm{d}z + K_{\mathrm{re}}\mathrm{d}z, \\ \mathrm{d}F_{\mathrm{a}}(\varphi,z) = K_{\mathrm{ac}}h[\varphi(z)]\mathrm{d}z + K_{\mathrm{ae}}\mathrm{d}z, \end{cases} \tag{1}$$

where $\mathrm{d}F_{\mathrm{t}}(\varphi,z)$ is the tangential force on the microelement cutting edge; $\mathrm{d}F_{\mathrm{r}}(\varphi,z)$ is the radial force on the microdimensional cutting edge; $\mathrm{d}F_{\mathrm{a}}(\varphi,z)$ is the axial force on the cutting edge of a microelement; K_{tc}, K_{rc}, and K_{ac} are the shear coefficients in all directions; K_{te}, K_{re}, and K_{ae} are the edge force coefficients in all directions; and $h[\varphi(z)]$ is the undeformed chip thickness.

The undeformed chip thickness, $h[\varphi(z)]$, varies periodically during the cutting process, and it can be expressed as follows [32]:

$$h[\varphi(z)] = f_{\mathrm{t}}\sin\varphi(z), \tag{2}$$

where f_{t} is the feedrate, and $\varphi(z)$ is the transient tooth position angle.

Substituting Eq. (2) into Eq. (1),

$$\begin{cases} \mathrm{d}F_{\mathrm{t}}(\varphi,z) = [K_{\mathrm{tc}}\sin\varphi(z) + K_{\mathrm{te}}]\mathrm{d}z, \\ \mathrm{d}F_{\mathrm{r}}(\varphi,z) = [K_{\mathrm{rc}}\sin\varphi(z) + K_{\mathrm{re}}]\mathrm{d}z, \\ \mathrm{d}F_{\mathrm{a}}(\varphi,z) = [K_{\mathrm{ac}}\sin\varphi(z) + K_{\mathrm{ae}}]\mathrm{d}z. \end{cases} \tag{3}$$

The instantaneous tooth position angle is calculated by the following equation:

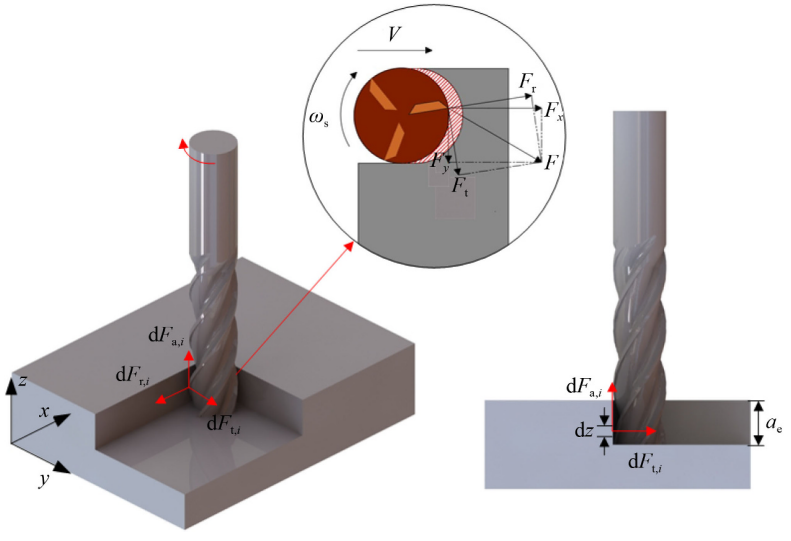

Fig. 1 Force diagram of the milling microelements.

$$\varphi(z) = \varphi_0 - \frac{2z\tan\eta}{r_d}, \tag{4}$$

where φ_0 is the radial position angle of the cutting edge microelement, and η is the helix angle.

When the instantaneous tooth position angle falls within the range $\varphi_{st} \leqslant \varphi \leqslant \varphi_{ex}$, the cutting edge is only milled to generate cutting force. The cut-in and cut-out angles for reverse milling and forward milling can be calculated using Eqs. (5) and (6), respectively:

$$\begin{cases} \varphi_{st} = 0, \\ \varphi_{ex} = \arccos\left(\dfrac{r_d - \alpha_p}{r_d}\right), \end{cases} \tag{5}$$

$$\begin{cases} \varphi_{st} = \dfrac{\pi}{2} + \arcsin\left(\dfrac{r_d - \alpha_p}{r_d}\right), \\ \varphi_{ex} = \pi, \end{cases} \tag{6}$$

where φ_{st} is the angle of incision of the tool, φ_{ex} is the cutting-out angle of the tool, and α_p is the radial depth of the cut.

The transformation relationship between the cutting microelement force in the machining coordinate system and the microelement force in the tangential coordinate system can be expressed as follows:

$$\begin{bmatrix} \mathrm{d}F_x(\varphi,z) \\ \mathrm{d}F_y(\varphi,z) \\ \mathrm{d}F_z(\varphi,z) \end{bmatrix} = \begin{bmatrix} -\cos\varphi(z) & -\sin\varphi(z) & 0 \\ \sin\varphi(z) & -\cos\varphi(z) & 0 \\ 0 & 0 & 1 \end{bmatrix} \begin{bmatrix} \mathrm{d}F_t(\varphi,z) \\ \mathrm{d}F_r(\varphi,z) \\ \mathrm{d}F_a(\varphi,z) \end{bmatrix}. \tag{7}$$

It can be obtained and simplified by substituting Eq. (3) into Eq. (7):

$$\begin{cases} \mathrm{d}F_x(\varphi,z) = \left\{ \dfrac{f_t}{2}\left[-K_{tc}\sin(2\varphi(z)) - K_{rc}(1-\cos(2\varphi(z)))\right] \right. \\ \qquad\qquad \left. + \left[-K_{te}\cos(\varphi(z)) - K_{re}\sin(\varphi(z))\right] \right\} \mathrm{d}z, \\ \mathrm{d}F_y(\varphi,z) = \left\{ \dfrac{f_t}{2}\left[K_{tc}(1-\cos(2\varphi(z))) - K_{rc}\sin(2\varphi(z))\right] \right. \\ \qquad\qquad \left. + \left[K_{te}\sin(\varphi(z)) - K_{re}\cos(\varphi(z))\right] \right\} \mathrm{d}z, \\ \mathrm{d}F_z(\varphi,z) = \left[K_{ac} f_t \sin(\varphi(z)) + K_{ae}\right] \mathrm{d}z. \end{cases} \tag{8}$$

When calculating the total cutting force, the microcutting force can be obtained by integrating it along the cutting edge.

2.2 Other evaluation parameters

As previously mentioned, the milling force is a key evaluation index that greatly affects the cutting heat, tool wear, machining accuracy, and surface quality of machined parts. During the machining process, an increase in cutting force accelerates the cutting edge speed and shortens the service life of the cutting edge, consequently affecting the surface quality of the machined parts [33–36]. The milling force serves as an indicator that reflects the milling conditions and the lubricating performance of various cutting oils. Improving lubrication performance reduces the cutting force, thereby enhancing cutting performance [37–39].

Moreover, the magnitude of the milling force primarily depends on the shear force coefficient of the material and the edge force coefficient during the cutting process. The shear force coefficient is determined by the workpiece material and remains constant throughout the machining process. The edge force coefficients (K_{te}, K_{re}, and K_{ae}) are influenced by friction between the cutting edge and the workpiece, chip, or plowing, with the coefficient of friction denoted as μ. Introducing lubricants and other lubrication methods effectively reduces friction, thereby minimizing the plowing phenomenon and decreasing the edge force coefficient. This ultimately reduces the overall cutting force and improves the quality of the workpiece processing. Consequently, the coefficient of friction serves as a crucial parameter for evaluating milling performance [40–42]. In actual machining, the coefficient of friction is indirectly calculated by measuring the milling force. The calculation of the coefficient of friction employs a different coordinate system from that of the milling force measurement, necessitating the conversion of coordinate system parameters [43,44]. The conversion equation is as follows:

$$\begin{bmatrix} F_r \\ F_t \end{bmatrix} = \begin{bmatrix} \sin(\gamma - \omega_s t) & -\cos(\gamma - \omega_s t) \\ \cos(\gamma - \omega_s t) & \sin(\gamma - \omega_s t) \end{bmatrix} \begin{bmatrix} F_x \\ F_y \end{bmatrix}, \tag{9}$$

where γ is the entrance angle, ω_s is the angular velocity, and t is the processing time.

The ratio of the normal force F_r, the tangential force F_t, and the friction coefficient μ, satisfy the following relationship:

$$\mu = \frac{F_r}{F_t}. \tag{10}$$

Additionally, milling performance can be evaluated by calculating the cutting specific energy. The cutting specific energy indicates the energy consumed to remove a unit volume of material and directly reflects the energy consumption level during machining [45–47]. This approach aids in obtaining a comprehensive understanding of the energy consumption formation mechanism and energy consumption calculation. The specific energy is primarily employed to assess machining efficiency, with lower cutting specific energy values indicating higher efficiency under the given conditions. The specific energy equation [42,48–50] is provided below:

$$U_W = \frac{P_z}{V_w} = \frac{F \cdot V}{\alpha_0 \cdot \alpha_e \cdot V_j}, \tag{11}$$

where U_W is the specific energy, P_z is the total energy consumed, V_w is the workpiece removal volume, V is the linear speed of the milling cutter, and F is the milling force.

The primary objective of milling is to achieve a high level of surface quality. Roughness plays a crucial role in evaluating the quality of part processing. Its value indicates the flatness of the processed surface, with a low roughness indicating a flat surface. The surface roughness of a workpiece directly impacts its fatigue strength, corrosion resistance, and compatibility with other components, thereby influencing its service life and reliability. The parameters used for surface evaluation include height characteristic parameters (Ra, Rz), spacing characteristic parameters (RSm), and shape characteristic parameters (Rmr) [51–53].

3 Evaluation experiments

3.1 Experimental equipment

For the milling and processing of the nickel-based alloy GH4169, the DGZX-10024/3.5U-KFHWJM three-axis spindle experimental platform was used. During the machining process, the milling force was measured by the LH-SZ-T05 piezoelectric three-axis force measuring instrument and then sent to the computer for data processing via the YC-02 three-axis force transducer. Once the milling process was completed, a TIME 3220 surface profiler was used to analyze the roughness of the milled workpiece surface. The experimental equipment and the analysis and measurement device are shown in Fig. 2, whereas the main parameters of the electric spindle are outlined in Table 1.

The electrostatic atomization working system comprises three main components: a high-voltage electrostatic generator, a microlubrication device, and a control system. A high-voltage electrostatic generator produces a stable and adjustable high-voltage electrostatic output. The microlubrication device controls the gas–liquid output. The control system, consisting of a microcontroller, serial touch screen, and information acquisition module, enables interaction between humans and machines, intelligent control of field parameters, and effective coordination of each functional partition through the establishment of a microcontroller, serial touch screen, and information acquisition module.

The workpiece material used is the nickel-based alloy GH4169, with dimensions of 40 mm × 25 mm × 6 mm. The chemical composition of the GH4169 nickel-based alloy can be found in Table 2, and its performance parameters are listed in Table 3. A tungsten steel alloy end milling cutter with a milling cutter head diameter of 4 mm, length of 12 mm, tool handle diameter of 4 mm, and total length of 50 mm was selected as the milling cutter.

For the EMQL lubrication media, the main components of soybean oil are fatty acids, as shown in Table 4, and the remaining fatty acids are undetected components of other species. Previous studies have demonstrated that polar functional groups such as –COOH and –COOR in

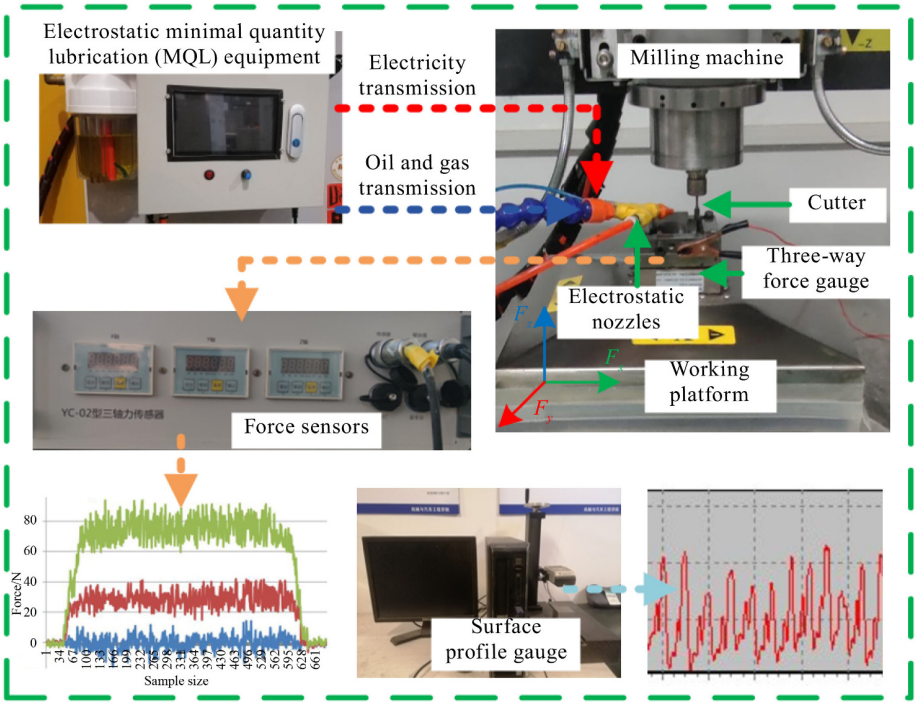

Fig. 2 Experimental equipment and measuring device.

Table 1 Main parameters of the experimental platform

Equipment parameter	Unit	Value
Spindle power	kW	4.2
Spindle torque	N·m	1.4
Cutting range	mm × mm × mm	100 × 100 × 30
Rated speed	$r \cdot min^{-1}$	24000

Table 2 Chemical composition of the GH4169 nickel-based alloy[a)]

Ni	C	Cr	Nb	Cu	Mo	Ti	Co	Mn	Al	Fe
50–55	0.08	17–21	5.25	0.3	3.1	0.96	1.0	0.35	0.95	Bal.

a): Unit = wt.%.

Table 3 Performance parameters of the GH4169 nickel-based alloy

Tensile strength/MPa	Yield strength/MPa	Elastic modulus/GPa	Hardness (HBS)	Density/ $(g \cdot cm^{-3})$
965	550	199.9	435	8.24

Table 4 Contents of various fatty acids in soybean oil[a)]

C14:0	C16:0	C18:0	C18:1	C18:2	C18:3	C20:0	C21:0	SFA	MUFA	PUFA
0.06	10.30	3.78	22.30	50.84	5.90	0.29	0.36	14.92	22.87	57.83

a): Quantities are in percentages.

soybean oil combine with metal surface molecules in grease through van der Waals forces, forming a lubricating and friction-reducing physical film [9,54–57]. Additionally, a chemisorption process occurs between soybean oil and the metal surface, also known as the "metal saponification reaction". This reaction forms a chemisorption film on the metal surface, providing lubrication and friction-reducing effects. Therefore, soybean oil is an ideal biodegradable base oil for MQL [58–60].

3.2 Experimental scheme

In each set of experiments, the sampling frequency of the dynamometer sensor was consistently set to 3 kHz, and the milling parameters remained the same, as shown in Table 5.

The objective of this experiment was to investigate the milling and lubrication performance under EMQL conditions. Using a univariate variable method, only the air pressure or voltage was changed in each group of experiments, while other experimental parameters were maintained at a flow rate of 100 $mL \cdot h^{-1}$, target distance of 50 mm, incident angle of 35°, and elevation angle of 50°. The results of the side milling comparison of the GH4169 nickel-based alloy were unchanged. Three sets of air pressures were used: 0.05, 0.5, and 0.15 MPa. The air pressure was constant within each group, and the voltage was adjusted according to a voltage gradient of 10 kV. A pure aerosol MQL test was conducted for each set of air pressure conditions for comparison to improve understanding. The experimental scheme is outlined in Table 6.

Table 5 Milling parameters

Milling parameter	Unit	Value
Milling type	–	Sideways milling
Milling cutter speed	$r \cdot min^{-1}$	9000
Milling cutter diameter	mm	4
Milling cutter helix angle	°	45
Radial depth of cut	μm	20
Axial depth of cut	mm	10
Feed rate	$mm \cdot min^{-1}$	100

Table 6 Experimental scheme of milling lubrication performance

Group	Barometric/MPa	Voltage/kV
No. 1	0.05	0
No. 2	0.05	20
No. 3	0.05	30
No. 4	0.05	40
No. 5	0.10	0
No. 6	0.10	20
No. 7	0.10	30
No. 8	0.10	40
No. 9	0.15	0
No. 10	0.15	20
No. 11	0.15	30
No. 12	0.15	40

3.3 Experimental results

3.3.1 Milling force

The variation in the typical directional milling force is shown in Fig. 3(a). The milling force fluctuated within the maximum peak value in all directions, with $F_y > F_x > F_z$ in terms of the peak size relationship. The fluctuation of the milling force in the z direction at 0 was negligible and could be disregarded.

Given that the milling force fluctuates during the milling process, it is typically evaluated based on the peak value. A data segment was selected for each set of milling force data, an equal number of milling force peaks was chosen, and their average value was calculated as the evaluation standard:

$$\bar{F}_{\max} = \frac{\sum_{i=1}^{N} F_{\max,i}}{N}, \tag{12}$$

where $F_{\max,i}$ is the ith milling force peak in the acquisition data, and $\bar{F}_{\max}$ is the average value.

The combined force of peak milling forces in all directions is

$$F = \sqrt{F_x^2 + F_y^2 + F_z^2}. \tag{13}$$

The anisotropic milling force data collected by the force measuring instrument were organized and calculated to identify the trend of milling force variations. Subsequently, data points were collected to calculate the average value. Figure 3(b) presents a bar graph illustrating the x and y milling separation forces, as well as the resultant force F.

As a result of the limited controllability of pure pneumatic MQL droplets, they tend to fly and drift, resulting in inadequate wetting performance in the machining area and increased cutting forces [61].

Under EMQL conditions, the milling force was significantly reduced. It reached its minimum when the voltage reached 30 kV under each air pressure condition. Compared with those under the pure pneumatic MQL condition at 0.05 MPa, F_x and F_y decreased by 40% and 9.5%, respectively, under the working condition of 30 kV/0.05 MPa. Additionally, the combined force decreased by 15.2%. Compared with those under the pure pneumatic MQL condition at 0.1 MPa, F_x and F_y decreased by 30% and 14%, respectively, under the working condition of 30 kV/0.1 MPa. The combined force decreased by 15.6%. Last, when compared with the pure pneumatic MQL condition at 0.15 MPa, F_x and F_y decreased by 26.7% and 14.6%, respectively, under the working condition of 30 kV/0.15 MPa. The combined force decreased by 15.9%.

As the voltage increased to 40 kV, the milling force increased to varying degrees under different air pressure conditions. During the experiment, discharge phenomena were observed between the nozzle electrode and the tool, workpiece, or worktable at a voltage of 40 kV. These events were attributed to the instability of the electric field distribution between the positive and negative electrodes caused by the discharge phenomena. Consequently, the transport performance of microliquid titration weakened, resulting in an increase in cutting force.

3.3.2 Friction coefficient and cutting specific energy

Using the measured milling force data and cutting parameters, the friction coefficient and cutting specific energy were calculated and plotted in Fig. 4. The trend of the friction coefficient and cutting specific energy followed a similar pattern to that of the cutting force. Under each air pressure, the values reached a relatively low level at a voltage of 30 kV. At 30 kV/0.15 MPa, the

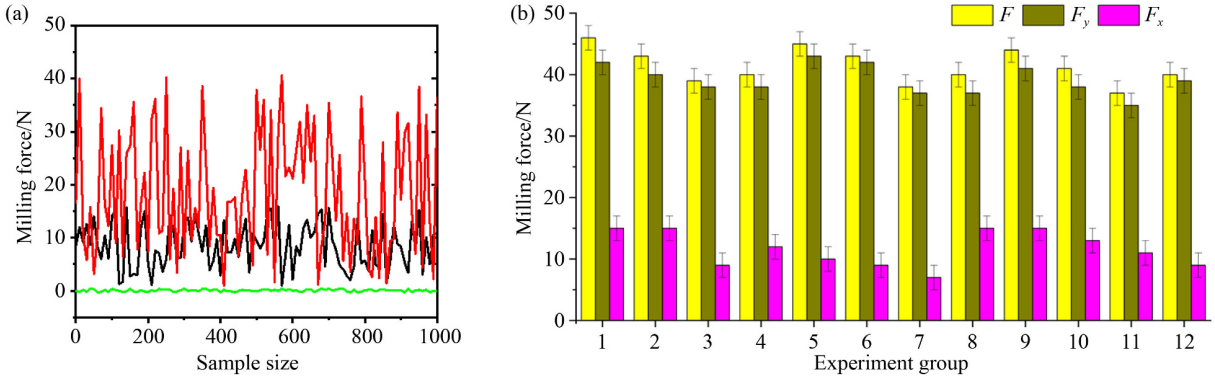

Fig. 3 (a) Typical milling force measurement signal diagram. (b) Milling component in the x and y directions and resultant force.

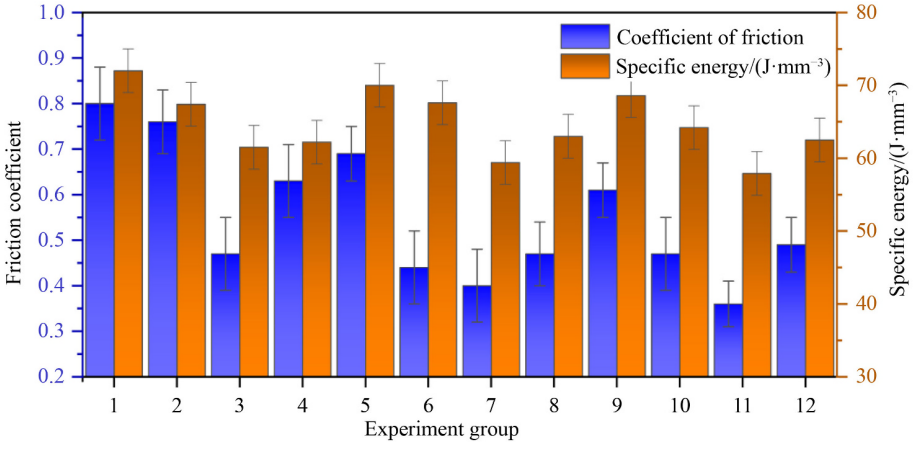

Fig. 4 Friction coefficient and cutting specific energy.

lowest friction coefficient and cutting specific energy were 0.36 and 57.9 J·mm^{-3}, respectively. These values represented decreases of 55% and 19.6% compared with the pure aerosol MQL condition at an air pressure of 0.05 MPa, indicating the excellent processing efficiency of EMQL technology in milling.

3.3.3 Surface quality of the workpieces

The surface quality of the measured surface was evaluated using two parameters: average distance Ra and average width RSm. The measured data were processed, and the experimental results are presented in Fig. 5.

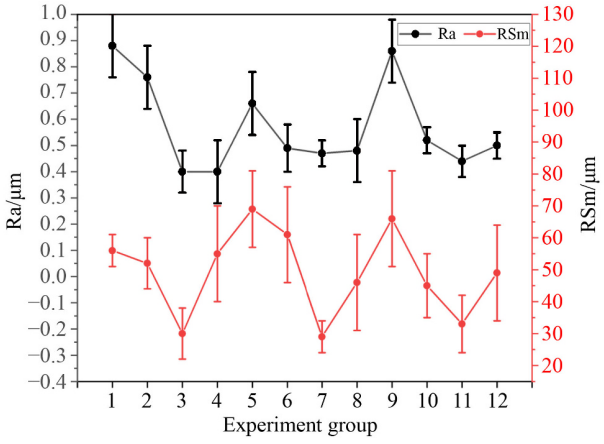

Fig. 5 Surface profile diagram of Ra and RSm values.

For the contour arithmetic mean deviation Ra value, the peaks were at 0.878 and 0.865 μm for the 0.05 and 0.15 MPa aerosols, respectively. The low air pressure at 0.05 MPa resulted in uneven atomization and insufficient infiltration of large droplets. At 0.15 MPa, we observed a tendency for droplet dispersion of the lubricant, leading to weakened lubrication performance in both cases. The Ra value obtained under EMQL conditions was lower than that under pure pneumatic MQL conditions. Under a voltage of 30 kV and air pressures of 0.05, 0.1, and 0.15 MPa, the Ra values decreased by 54.2%, 30.9%, and 52%, respectively, whereas the RSm values decreased by 47.4%, 58.3%, and 48.8%, respectively.

On the basis of the comparison of the experimental data above, the following conclusions were drawn: the three-way milling force, resultant force, friction coefficient, cutting specific energy, and surface roughness were reduced compared with those under pure aerosol MQL lubrication. In terms of voltage, most of the characteristic parameters decreased first and then slightly increased as the voltage increased. When the voltage reached 30 kV, the machining quality was optimal. This result indicated that EMQL technology was suitable for a certain voltage threshold, as excessive voltage could affect the electric field distribution and result in decreased lubrication performance.

3.4 Analysis and discussion

3.4.1 Surface autocorrelation analysis

The application of the cross-correlation function to the microscopic analysis of the surface mass of the part could be used to characterize the similarity of the differential displacement τ of the two waveforms and reveal the isotropy and anisotropy of the shape of the processed surface under different lubrication conditions. Meanwhile, the autocorrelation function represents the similarities when the same profile waveform shifts τ [62,63]. Given the absence of a clear reference group for surface quality in this experiment, the optimal solution could not be obtained. Therefore, the surface profile was further compared using only the autocorrelation function, which can be expressed by the following equation [64]:

$$R_x(\tau) = \frac{1}{L}\int_0^L x(t)\,x(t+\tau)\,\mathrm{d}t, \tag{14}$$

where $x(t)$ and $x(t+\tau)$ are the distances between the surface contour and the centerline of t and $t+\tau$, respectively.

The digital estimation equation is as follows [62]:

$$\mathrm{ACF}(rh_c) = \frac{1}{N-r}\sum_{n=0}^{N_m-r-1} Y_n Y_{n+r},\ r = 0,1,2,\ldots,m,\ m < n, \tag{15}$$

where r is the number of transverse displacements, m is the maximum number of lateral shifts, N_m is the sampling capacity, h_c is the sampling interval, Y_n is the height of the contour at n, and Y_{n+r} is the height of the profile at $n + r$.

As a measure of the similarity in the surface topography of the workpiece, the autocorrelation function generally reaches its maximum at $\tau = 0$. Additionally, the waveform characteristics of the autocorrelation function differ for various profiles. As τ increases, the autocorrelation function of the random profile gradually decreases until it approaches zero. By contrast, the autocorrelation function remains in a stable oscillation state. The autocorrelation coefficient of the profile in the random profile changes over time until it reaches a stable cycle. This allows for the assessment of whether the contour contains periodic patterns and enables a comparison of the frequencies of different contour curves to comprehensively evaluate the surface quality of the workpiece.

The surface data of the specimens in the three sets of experiments (30 kV/0.05 MPa, 30 kV/0.1 MPa, and 30 kV/0.15 MPa) were integrated and analyzed in accordance with the autocorrelation equation, as depicted in Fig. 6. The autocorrelation function curves in all three states showed a maximum value near 0 and decreased

over time until approaching zero. The 30 kV/0.05 MPa condition yielded a large longitudinal parameter value for the surface contour. At 30 kV/0.1 MPa, the digital estimation of the autocorrelation function value was slightly low, but the surface profile exhibited obvious periodicity, better surface contour curve uniformity, a more regular contour curve on the workpiece surface, and a higher surface line support rate compared with those under the two other conditions. By considering the specific data on the milling force and friction coefficient, we concluded that the application of EMQL technology in milling processing could achieve high processing quality at 30 kV/0.1 MPa.

3.4.2 Electrostatic atomization lubrication mechanism and gain analysis

Through the analysis of the aforementioned experiments and their results, we found that the applied electric field had a substantial effect on enhancing the quality of the process. However, further examination of the lubrication mechanism is necessary to establish a theoretical foundation for the application of EMQL technology. In comparison with conventional MQL technology, EMQL technology primarily differs in terms of spray characteristics (such as package deposition performance, particle size, and distribution) and droplet characteristics, whether they are charged or not [65–68].

The spray characteristics play a crucial role in determining the lubrication and cooling properties. Through electrostatic spraying, the minute water droplets emitted from microlubrication are easily transported to the cutting area, thereby establishing a dense and stable lubrication layer in that region. This is particularly significant due to the intense friction between the tool and the workpiece, as well as the formation of chips, which generate a large number of capillaries in the sliding contact area. These capillaries act as conduits for the cutting fluid, improving the friction behavior between the tool and the chip interface. The reduction in the surface tension of charged droplets enhances their capillary driving force, thereby facilitating the filling of capillaries by the cutting fluid.

As depicted in Fig. 7, while keeping the nozzle position and milling process parameters constant, the lubrication characteristics of electrostatic spraying between milling areas are closely correlated with the average volume of droplets, air pressure, and voltage, which are key factors influencing electrostatic spraying. Consequently, small particle sizes allow easy transport to the tool/workpiece and tool/chip interfaces, resulting in improved permeability. Additionally, under the influence of an external electric field, small droplet sizes exhibit enhanced heat transfer capabilities, leading to high heat flux efficiency [35,69].

However, the increase in machining quality is not solely determined by voltage. The suitability of EMQL technology depends on a specific voltage threshold. When the voltage reaches 40 kV, the gas between the plate electrodes breaks down, resulting in gas discharge phenomena such as flash and burst sounds, as depicted in Fig. 8. This discharge phenomenon is essentially a spark-like tip discharge, similar to lightning, which occurs only when the voltage reaches a certain threshold. At low voltages, a corona-like tip discharge, localized near the electrode tip, occurs. The corona generated by the electrode causes ionization of the air in the nearby region, producing ionized wind that emits a hissing sound and weak fluorescence [70].

In the application of EMQL, corona discharge plays a critical role, with the electrodes maintained in a relative electric balance state. The air in the electric field region becomes ionized, and mist droplets become charged through contact or corona discharge. These charged droplets are then transported in an orderly manner to the cutting area under the influence of the electrostatic field. In the state of electrostatic equilibrium, the strength of the electric field surrounding the conductor is linearly related

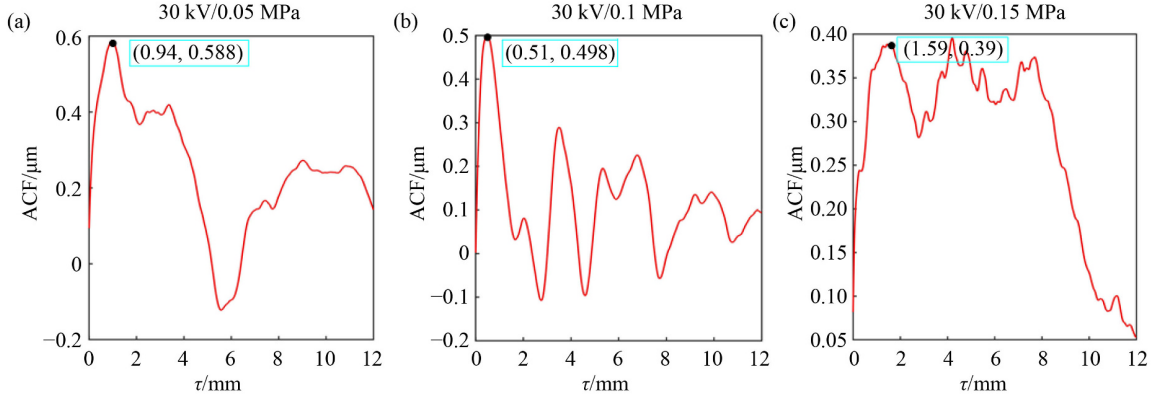

Fig. 6 Autocorrelation function curve (ACF) of the workpiece contour surface.

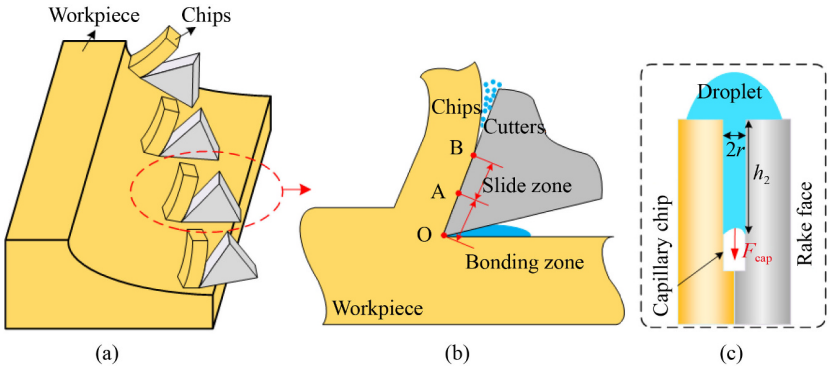

Fig. 7 (a–c) Microaction mechanism of charged droplets in the cutting process.

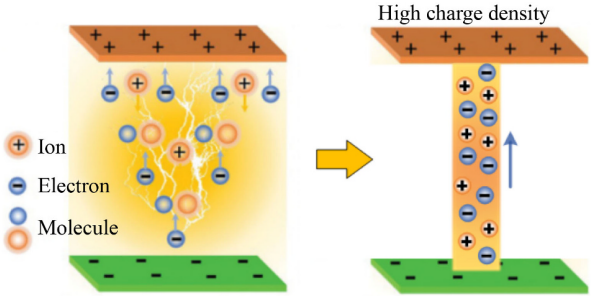

Fig. 8 Mechanism of the increasing and decreasing benefits of the electric field.

to the surface charge density of the conductor. The protruding and sharp parts of a conductor, characterized by tips with large curvatures, exhibit high charge densities and increased surface charge density. Consequently, the surrounding field strength increases, with the voltage playing a positive feedback role in the transport of droplets.

Under normal atmospheric pressure, when a high voltage is applied between two electrodes, spark discharge occurs, resulting in the formation of a narrow, curved channel between the two electrodes. This phenomenon occurs when the air transitions from being an insulator to becoming a good conductor due to its destruction, leading to a rapid increase in current. If the power supply is not overly high, the voltage decreases after discharge, causing the discharge to temporarily cease. Once the voltage recovers, a discharge occurs again, resulting in a pulse discharge phenomenon. This leads to a decrease in charge density in the surrounding area, disruption of the stable distribution of the original electric field, and deterioration of the control of microdroplets. As the voltage continues to increase, the severity of the spark discharge intensifies. Excessive voltage can cause issues such as thermal expansion of the electrode and workpiece, electrode polarization phenomenon, which subsequently affects the quality of machining, and damage to the discharge equipment.

4 Evaluation and optimization experiments

4.1 Experimental equipment

The equipment used in this experiment included a DGZX-10024/3.5U-KFHWJM electrospinning experimental platform, an EMQL delivery device, an LH-SZ-T05 piezoelectric three-direction force measuring instrument, a YC-02 three-axis force transducer, a TIME 3220 surface profile instrument, and a laser confocal microscope for surface morphology data acquisition, as depicted in Fig. 9.

The experimental materials utilized were as follows: GH4169 nickel base alloy, with dimensions of 40 mm × 25 mm × 6 mm; tungsten steel alloy micro diameter milling cutter, with dimensions of 4 mm (Φ) ×12 mm (C) × 50 mm (L) × 4 mm (D); and biolubricant soybean oil.

4.2 Experimental scheme

The objective of this experimental research was to optimize the combination of various jet parameters and position parameters. The factors considered were the flow rate, air pressure, voltage, incident angle, elevation angle, and target distance. Gas and voltage were set at three levels, whereas the other factors were kept as consistent as possible. The levels of each factor are detailed in Table 7.

Therefore, an L18(3^7) orthogonal table was selected to merge the interactions between different factors into an error. The factor-level arrangement is presented in Table 8. During the experiment, the milling performance parameters of the EMQL were optimized using the signal-to-noise ratio objective function, which was based on the measured cutting force, cutting specific energy, and surface morphology.

4.3 Experimental results analysis

4.3.1 Signal-to-noise ratio analysis

The signal-to-noise (S/N) ratio is used as a measure of

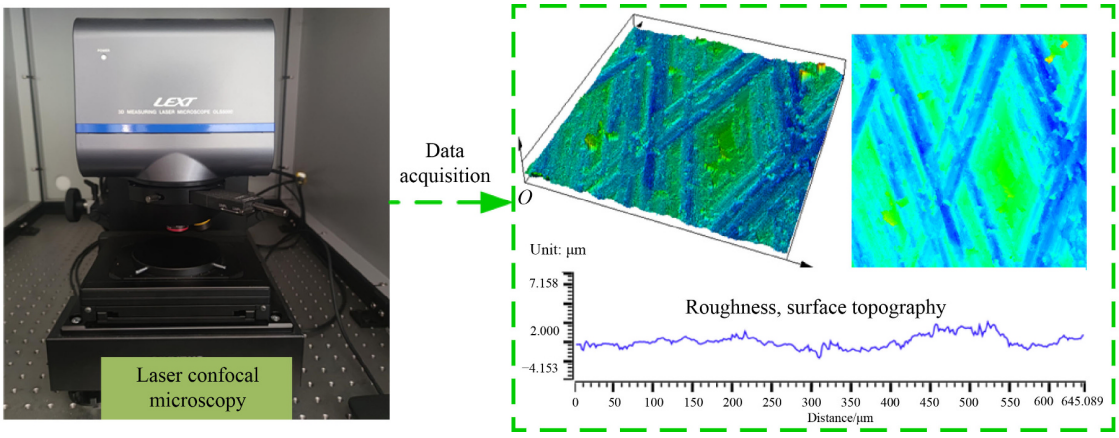

Fig. 9 Laser confocal microscopy.

Table 7 Orthogonal experiment factor levels

Factor	Unit	Level 1	Level 2	Level 3
Flow rate, A	$mL \cdot h^{-1}$	60	80	100
Barometric, B	MPa	0.05	0.10	0.15
Voltage, C	kV	20	30	40
Angle of incidence, D	°	15	35	55
Azimuthal angle, E	°	30	50	70
Target distance, F	mm	30	40	50

deviation from the desired values, with performance characteristics of smaller-the-better, nominal-the-better [30], and larger-the-better. In this experiment, the objective was to obtain low values of force, specific energy, and surface roughness. Therefore, the smaller-the-better characteristic was utilized.

Regardless of the S/N performance properties, the combination of experimental factors with the highest S/N values will yield the smallest variance, indicating better cutting quality [71]. Thus, the horizontal combination

Table 8 Experimental scheme[a)]

No.	A	B	C	D	E	F	Error	Experimental program					
	1	2	3	4	5	6	7	A	B	C	D	E	F
1	1	1	1	1	1	1	1	60	0.05	20	15	30	30
2	1	2	2	2	2	2	2	60	0.10	30	35	50	40
3	1	3	3	3	3	3	3	60	0.15	40	55	70	50
4	2	1	1	2	2	3	3	80	0.05	20	35	50	50
5	2	2	2	3	3	1	1	80	0.10	30	55	70	30
6	2	3	3	1	1	2	2	80	0.15	40	15	30	40
7	3	1	2	1	3	2	3	100	0.05	30	15	70	40
8	3	2	3	2	1	3	1	100	0.10	40	35	30	50
9	3	3	1	3	2	1	2	100	0.15	20	55	50	30
10	1	1	3	3	2	2	1	60	0.05	40	55	50	40
11	1	2	1	1	3	3	2	60	0.10	20	15	70	50
12	1	3	2	2	1	1	3	60	0.15	30	35	30	30
13	2	1	2	3	1	3	2	80	0.05	30	55	30	50
14	2	2	3	1	2	1	3	80	0.10	40	15	50	30
15	2	3	1	2	3	2	1	80	0.15	20	35	70	40
16	3	1	3	2	3	1	2	100	0.05	40	35	70	30
17	3	2	1	3	1	2	3	100	0.10	20	55	30	40
18	3	3	2	1	2	3	1	100	0.15	30	15	50	50

a): First eight columns are factorial arrangements.

corresponding to the highest S/N value was regarded as the optimal combination. The collected data from each group of experiments were sorted, and the corresponding S/N ratios were calculated. The results are presented in Table 9.

Each characterization parameter was plotted separately as a main effect map using the data from Table 9. Figures 10 and 11 display the main effect diagrams of each factor corresponding to the cutting force and specific energy index, respectively. The influence of each factor on the milling force and cutting specific energy was generally consistent. The optimal combination was A2B2C2D2E1F2, with a corresponding experimental indicator of a flow rate of 80 mL·h^{-1}, an air pressure of 0.1 MPa, a voltage of 30 kV, an incident angle of 35°, an elevation angle of 30°, and a target distance of 40 mm.

Figure 12 depicts the main effect graph of each factor corresponding to the roughness index. The optimal combination was A3B2C2D2E3F2, and the corresponding experimental parameters were a flow rate of 100 mL·h^{-1}, an air pressure of 0.1 MPa, a voltage of 30 kV, an incident angle of 35°, an elevation angle of 70°, and a target distance of 40 mm.

Table 9 Experimental results and signal-to-noise (S/N) ratio[a)]

No.	F/N	U/(J·mm^{-3})	Ra/μm	S/N$_F$	S/N$_U$	S/N$_{Ra}$
1	43.68	68.61	0.71	−32.81	−36.73	2.94
2	37.82	59.41	0.44	−31.55	−35.48	7.23
3	44.82	70.40	0.67	−33.03	−36.95	3.49
4	42.97	67.50	0.73	−32.67	−36.59	2.70
5	39.58	62.17	0.40	−31.95	−35.87	8.02
6	40.36	63.40	0.52	−32.12	−36.04	5.73
7	40.87	64.20	0.49	−32.23	−36.15	6.23
8	41.62	65.38	0.62	−32.39	−36.31	4.14
9	43.04	67.61	0.70	−32.68	−36.60	3.11
10	47.26	74.24	0.72	−33.49	−37.41	2.91
11	40.08	62.96	0.49	−32.06	−35.98	6.14
12	44.56	70.00	0.41	−32.98	−36.90	7.74
13	37.88	59.50	0.44	−31.57	−35.49	7.11
14	42.96	67.48	0.53	−32.66	−36.58	5.53
15	39.77	62.47	0.45	−31.99	−35.91	6.92
16	40.73	63.98	0.43	−32.20	−36.12	7.27
17	39.17	61.53	0.32	−31.86	−35.78	9.87
18	45.44	71.38	0.45	−33.15	−37.07	6.94

a): Unit of S/N = dB.

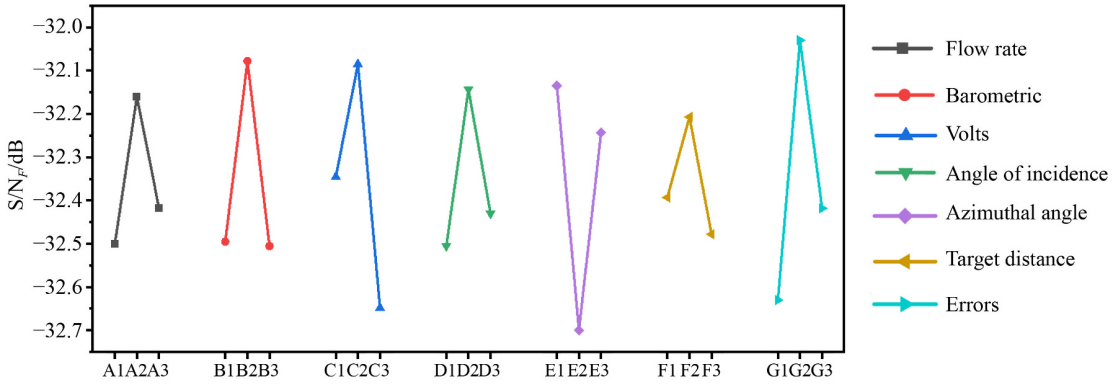

Fig. 10 Effect curve of each factor corresponding to the milling force index.

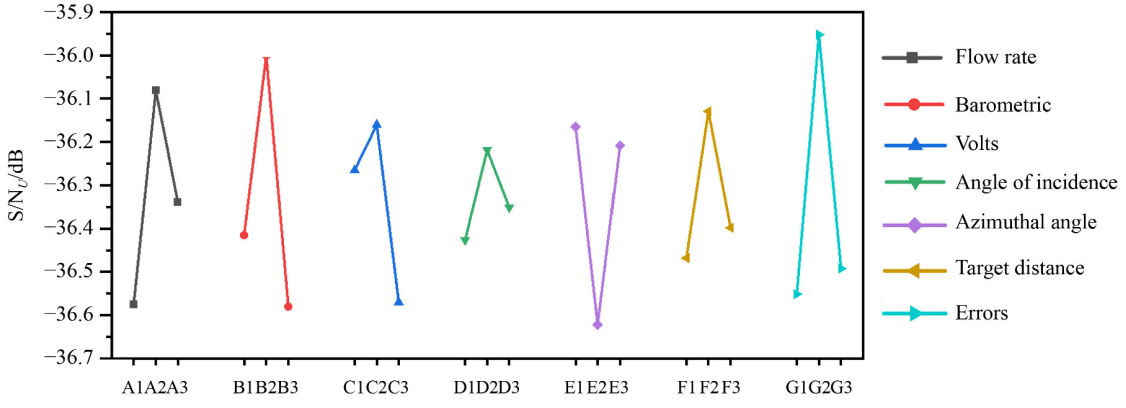

Fig. 11 Effect curve of each factor corresponding to the cutting specific energy index.

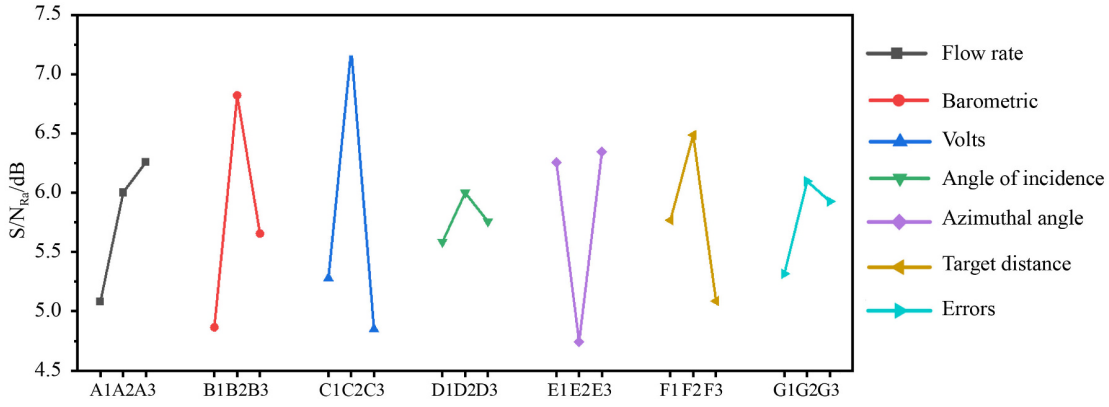

Fig. 12 Effect curve of each factor corresponding to the roughness index.

4.3.2 Analysis of variance

The analysis of variance aims to identify the level of factors that significantly impact the characteristic parameters of milling performance [72]. In this analysis, the degrees of freedom for each factor were calculated as the number of levels of the factor minus 1, based on the orthogonal table used in the experiment. Given that the orthogonal test in this study consisted of three levels, the degrees of freedom for the factors and error in this experiment were both 2. The cutting force, cutting specific energy, and surface roughness were analyzed individually, and the results are presented in Table 10. Figure 13 shows the contribution ratio of each factor in terms of the force, specific energy, and surface roughness. Each factor had a similar effect on the force and cutting specific energy. The air pressure exerted the greatest influence, accounting for approximately 22%, followed by the elevation angle with a contribution rate of approximately 16%. The incidence angle had the smallest impact, with a contribution rate of approximately 3%. Other factors, such as voltage, flow rate, and target distance, contributed approximately 16%, 11%, and 7%, respectively, to the force and cutting specific energy.

Regarding surface roughness, the voltage factor had the greatest impact, contributing 36.71%. The air pressure factor ranked next with a contribution rate of 21.26%. The incident angle factor had the smallest impact, with a contribution rate of 0.97%. Other factors, namely, the flow rate, elevation angle, and target distance, contributed 8.7%, 18.84%, and 9.18%, respectively, to the surface roughness. The analysis revealed that the electrostatic field significantly improved the surface quality of the workpiece.

Table 10 Variance analysis results of the force, specific energy, and surface roughness

Source of variance	Factor	Square sum	Mean square	*F*-value
Force, *F*/N	A	17.96	8.98	1.30
	B	25.03	12.51	1.94
	C	12.37	6.18	0.85
	D	3.09	1.55	0.20
	E	18.76	9.38	1.37
	F	8.14	4.07	0.54
	Error	30.40	15.20	2.49
	S_T	115.74		
Specific cutting energy, U/(J·mm^{-3})	A	44.43	22.22	1.30
	B	61.67	30.84	1.94
	C	30.55	15.27	0.85
	D	7.68	3.84	0.20
	E	46.25	23.13	1.36
	F	20.11	10.05	0.54
	Error	74.92	37.46	2.49
	S_T	285.61		
Surface roughness, Ra/μm	A	0.02	0.01	0.50
	B	0.04	0.02	1.39
	C	0.08	0.04	2.77
	D	0.01	0.01	0.06
	E	0.04	0.02	1.18
	F	0.02	0.01	0.55
	Error	0.01	0.01	0.25
	S_T	0.21		

4.3.3 Confirmatory experimental analysis

The aforementioned analysis revealed that the minimum milling force and cutting specific energy were achieved with a flow rate of 80 mL·h^{-1}, pressure of 0.1 MPa, voltage of 30 kV, incident angle of 35°, elevation angle of 30°, and target distance of 40 mm. Additionally, the best surface quality was obtained with a flow rate of 100 mL·h^{-1}, pressure of 0.1 MPa, voltage of 30 kV, incident angle of 35°, elevation angle of 70°, and target distance of 40 mm. These two parameter sets were not included in the orthogonal experimental group; thus,

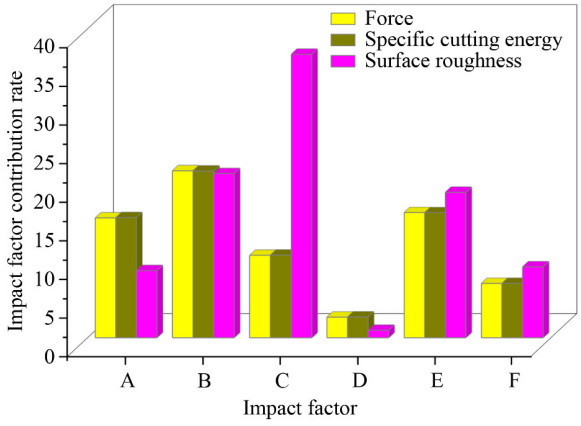

Fig. 13 Contribution ratio of each factor to the force, specific energy, and surface roughness.

confirmatory experimental analysis was required to validate the optimal combination of EMQL process parameters.

Initially, the milling force and cutting specific energy were measured with the combined parameters of flow rate (80 mL·h^{-1}), air pressure (0.1 MPa), voltage (30 kV), incident angle (35°), elevation angle (30°), and target distance (40 mm). The obtained force and specific energy were 36.75 N and 57.73 J·mm^{-3}, respectively. Notably, these values were lower than the orthogonal experimental values of each group.

The experimental results of the combined parameters of flow rate (100 mL·h^{-1}), air pressure (0.1 MPa), voltage (30 kV), incidence angle (35°), elevation angle (70°), and target distance (40 mm) indicated a surface roughness of 0.275 μm for the workpiece. Similarly, this value was lower than the roughness observed in the orthogonal experiment of each group. Therefore, the aforementioned analyses regarding the force, specific energy, and roughness are accurate.

To further compare the lubrication performance of EMQL milling under a combination of these two parameters, we presented the surface morphology of the workpiece under the two working conditions. Additionally, multiple groups of surface morphologies were selected in the orthogonal experimental group, as shown in Fig. 14. The machining conditions shown in Fig. 14(a) were as follows: flow rate of 80 mL·h^{-1}, air pressure of 0.1 MPa, voltage of 30 kV, incidence angle of 35°, elevation angle of 30°, and target distance of 40 mm. Figure 14(b) shows a flow rate of 100 mL·h^{-1}, an air pressure of 0.1 MPa, a voltage of 30 kV, an incidence angle of 35°, an elevation angle of 70°, and a target distance of 40 mm.

The processing surface under the preferred parameter combination of the two groups was relatively flat, with fewer defects, such as slips and cracks. Conversely, the surface morphology of the workpiece in the orthogonal test group showed a large amount of peeling, microchipping, abrasion, and other injuries, indicating poor processing quality. An increase in liquid flow might result in insufficient atomization of the lubricant, leading to an increase in the displacement of small droplets. Such a scenario could cause harm to the surrounding environment and the staff. After conducting a comprehensive analysis, the optimal parameter combination for EMQL was determined as follows: a flow rate of 80 mL·h^{-1}, an air pressure of 0.1 MPa, a voltage of 30 kV, an incidence angle of 35°, an elevation angle of 30°, and a target distance of 40 mm.

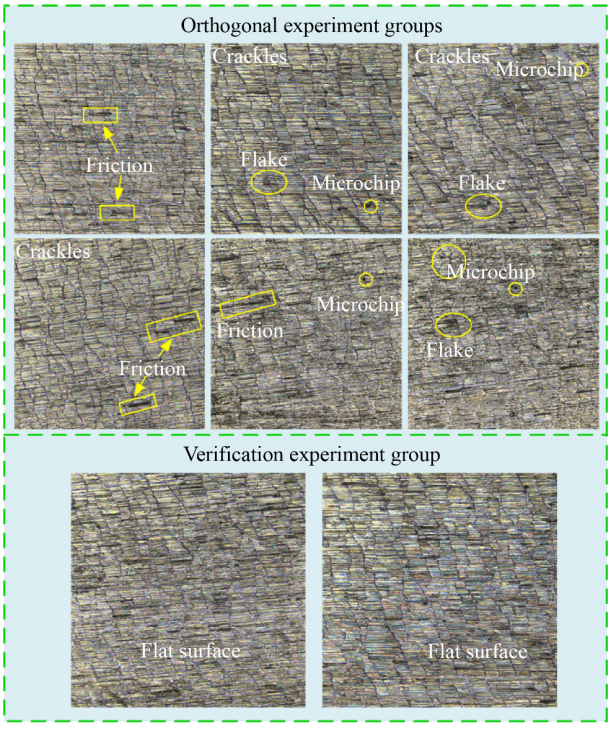

Fig. 14 Surface topography of the workpiece under different working conditions.

5 Conclusions

To investigate the effects of the electric field parameters and nozzle position parameters on the milling force, cutting specific energy, and surface roughness, we evaluated and optimized the milling performance. The following conclusions were drawn:

(1) Compared with pure pneumatic atomized milling, electrostatic atomization-assisted aerosols demonstrated better milling performance, reducing the milling force by 15.2%, 15.6%, and 15.9% at air pressures of 0.05, 0.1, and 0.15 MPa, respectively. Moreover, the friction coefficient and cutting ratio energy were the lowest under 30 kV/0.15 MPa lubrication, decreasing by 55% and 19.6%, respectively, compared with those under pure aerosol MQL with an air pressure of 0.05 MPa.

(2) Compared with those of the pure pneumatic MQL

milling with air pressures of 0.05, 0.1, and 0.15 MPa, the Ra values of the workpiece under EMQL (30 kV) conditions decreased by 54.2%, 30.9%, and 52%, respectively, whereas the RSm values decreased by 47.4%, 58.3%, and 48.8%, respectively.

(3) The minimum milling force and cutting specific energy were achieved with a flow rate of 80 mL·h^{-1}, a pressure of 0.1 MPa, a voltage of 30 kV, an incident angle of 35°, an elevation angle of 30°, and a target distance of 40 mm. The best surface quality was obtained using a flow rate of 100 mL·h^{-1}, a pressure of 0.1 MPa, a voltage of 30 kV, an incident angle of 35°, an elevation angle of 70°, and a target distance of 40 mm.

(4) The most significant influence on milling force and cutting specific energy was air pressure, with a contribution rate of 22%. Then, the elevation angle was 16%. The effects of the voltage, flow rate, target distance, and incident angle on the force and cutting specific energy were 16%, 11%, 7%, and 3%, respectively.

(5) In terms of surface roughness, the voltage factor had the greatest impact, contributing 36.71%. Air pressure followed, with a contribution rate of 21.26%. The effects of the flow rate, elevation angle, target distance, and incident angle on the surface roughness were 8.7%, 18.84%, 9.18%, and 0.97%, respectively.

(6) Considering the impact of droplet atomization and flight dispersion on the environment and human health, the optimal parameters for EMQL were ultimately determined to be a flow rate of 80 mL·h^{-1}, an air pressure of 0.1 MPa, a voltage of 30 kV, an incident angle of 35°, an elevation angle of 30°, and a target distance of 40 mm.

Nomenclature

Abbreviations

ACF	Autocorrelation function curve
EMQL	Electrostatic atomization minimum quantity lubrication
MQL	Minimal quantity lubrication
S/N	Signal-to-noise

Variables

$\mathrm{d}F_{\mathrm{a}}(\varphi, z)$	Axial force on the micro cutting edge
$\mathrm{d}F_{\mathrm{t}}(\varphi, z)$	Tangential force on the micro cutting edge
$\mathrm{d}F_{\mathrm{r}}(\varphi, z)$	Radial force on the microdimensional cutting edge
$\mathrm{d}z$	Thickness of the cutting edge micro element
F	Milling force
$\bar{F}_{\max}$	Mean value
$F_{\max,i}$	Peak milling force of the ith milling force in the collected data
f_{t}	Feed rate
$h[\varphi(z)]$	Undeformed chip thickness
h_{c}	Sampling interval
K_{te}, K_{re}, K_{ae}	Edge force coefficient in each direction
K_{tc}, K_{rc}, K_{ac}	Coefficient of shear force in all directions
L	Sampling length
m	Maximum number of transverse displacements
n	Number of data obtained
N_m	Sampling capacity
P_{z}	Total energy consumed
r	Number of transverse displacements
Ra	Arithmetic mean deviation of surface profile
RSm	Average width of surface contour lines
t	Machining time
U_{W}	Specific energy
V	Milling tool linear speed
V_{j}	Area swept by the milling cutter on the workpiece surface per unit time
V_{w}	Workpiece removal volume
$x(t)$, $x(t+\tau)$	Distance between surface contour and centerline at t and $t + \tau$
y_i	Actual sample data obtained
Y_n	Height value of the nth contour
Y_{n+r}	Height value of the contour at $(n + r)$th place
$Z(x)$	Arithmetic mean of contour height
α_{p}	Radial depth of cut
γ	Angle of incision
ω_{s}	Angular velocity
η	Helix angle
φ_0	Angle of radial position of the cutting edge micro element
φ_{ex}	Angle of incision of the tool
φ_{st}	Angle of incision of the tool
$\varphi(z)$	Instantaneous tooth position angle

Acknowledgements This study was financially supported by the National Natural Science Foundation of China (Grant No. 52205481), the Support Plan for Outstanding Youth Innovation Team in Universities of Shandong Province, China (Grant No. 2023KJ114), and the Qingdao Science and Technology Planning Park Cultivation Plan, China (Grant No. 23-1-5-yqpy-17-qy).

Conflict of Interest Changhe LI is a member of the Editorial Board of *Frontiers of Mechanical Engineering*, who was excluded from the peer review process and all editorial decisions related to the acceptance and publication of this article. Peer review was handled independently by the other editors to minimize bias.

References

1. Tian W, Chang S, Zhou C S, Zhang W D, Feng Z H, Sun X Y, Su R. Microstructure transformation and metallographic analysis of nickel-based wrought superalloy during heat treatment. Heat Treatment of Metals, 2021, 46(8): 30–35 (in Chinese)

2. Xu W H, Li C H, Cui X, Zhang Y B, Yang M, Gao T, Liu M Z, Wang X M, Zhou Z M, Sharma S, Dambatta Y S. Atomization mechanism and machinability evaluation with electrically charged nanolubricant grinding of GH4169. Journal of Manufacturing Processes, 2023, 106: 480–493
3. Gong P, Zhang Y B, Wang C J, Cui X, Li R Z, Sharma S, Liu M Z, Gao T, Zhou Z M, Wang X M, Dambatta Y S, Li C H. Residual stress generation in grinding: mechanism and modeling. Journal of Materials Processing Technology, 2024, 324: 118262
4. Song Y X, Li C H, Zhou Z M, Liu B, Sharma S, Dambatta Y S, Zhang Y B, Yang M, Gao T, Liu M Z, Cui X, Wang X M, Xu W H, Li R Z, Wang D Z. Nanobiolubricant grinding: a comprehensive review. Advances in Manufacturing, 2024
5. Hu S G, Li C H, Li B K, Yang M, Wang X M, Gao T, Xu W H, Dambatta Y S, Zhou Z M, Xu P M. Digital twins enabling intelligent manufacturing: from methodology to application. Intelligent and Sustainable Manufacturing, 2024, 1(1): 10007
6. Dambatta Y S, Li C H, Sayuti M, Sarhan A A D, Yang M, Li B K, Chu A X, Liu M Z, Zhang Y B, Said Z, Zhou Z M. Grindability evaluation of ultrasonic assisted grinding of silicon nitride ceramic using minimum quantity lubrication based SiO_2 nanofluid. Chinese Journal of Mechanical Engineering, 2024, 37(1): 25
7. Shi Y X, Zhao B, Ding W F. Solid additives to increase the service life of ceramic cutting tool: methodology and mechanism. Intelligent and Sustainable Manufacturing, 2024, 1: (2): 10009
8. Xu X F, Lv T, Luan Z Q, Zhao Y Y, Wang M H, Hu X D. Capillary penetration mechanism and oil mist concentration of Al_2O_3 nanoparticle fluids in electrostatic minimum quantity lubrication (EMQL) milling. The International Journal of Advanced Manufacturing Technology, 2019, 104(5–8): 1937–1951
9. Khosravi J, Azarhoushang B, Barmouz M, Bösinger R, Zahedi A. High-speed milling of Ti6Al4V under a supercritical CO_2+MQL hybrid cooling system. Journal of Manufacturing Processes, 2022, 82: 1–14
10. Gu G Q, Wang D Z, Wu S J, Zhou S, Zhang B X. Research status and prospect of ultrasonic vibration and minimum quantity lubrication processing of nickel-based alloys. Intelligent and Sustainable Manufacturing, 2024, 1(1): 10006
11. Kong K, Hu Z Q, Yao W Q, Huang S Q, Xu X F. Sizes distribution characteristics of cutting fluid droplets for electrostatic atomization minimum quantity lubrication. Journal of Mechanical & Electrical Engineering, 2013, 30(12): 1472–1476 (in Chinese)
12. Patel M K, Sharma T, Nayak M K, Ghanshyam C. Computational modeling and experimental evaluation of the effects of electrode geometry and deposition target on electrostatic spraying processes. International Journal of Computer Applications, 2015, 124(2): 10–15
13. Reddy N S K, Yang M. Development of an electrostatic lubrication system for drilling of SCM 440 steel. Proceedings of the Institution of Mechanical Engineers, Part B: Journal of Engineering Manufacture, 2009, 224(2): 217–224
14. Jiang H, Su Y. Study on atomization characteristics and machining performance of coaxial electrostatic atomization cutting. Modular Machine Tool & Automatic Manufacturing Technique, 2021, 6: 146–149 (in Chinese)
15. Tang Z C, Su Y. Investigation on co-axial electrostatic atomization cutting. Tool Engineering, 2018, 52(5): 51–55 (in Chinese)
16. Yang M, Hao J C, Wu W T, Li Z H, Ma Y Q, Zhou Z M, Gao T, Liu M Z, Cui X, Zhang Y B, Li B K, Ma X, Dambatta Y S, Li C H. Critical cutting thickness model considering subsurface damage of zirconia grinding and friction–wear performance evaluation applied in simulated oral environment. Tribology International, 2024, 198: 109881
17. Li C H. Thermodynamic Mechanism of MQL Grinding with Nano Bio-lubricant. Berlin: Springer, 2024, 43–115
18. Huang S Q, Lv T, Xu X F, Ma Y L, Wang M H. Experimental evaluation on the effect of electrostatic minimum quantity lubrication (EMQL) in end milling of stainless steels. Machining Science and Technology, 2018, 22(2): 271–286
19. Xu X F, Huang S Q, Wang M H, Yao W Q. A study on process parameters in end milling of AISI-304 stainless steel under electrostatic minimum quantity lubrication conditions. The International Journal of Advanced Manufacturing Technology, 2017, 90(1): 979–989
20. Huang S Q, Lv T, Wang M H, Xu X F. Enhanced machining performance and lubrication mechanism of electrostatic minimum quantity lubrication-EMQL milling process. The International Journal of Advanced Manufacturing Technology, 2018, 94(1): 655–666
21. Huang S Q, Lv T, Wang M H, Xu X F. Effects of machining and oil mist parameters on electrostatic minimum quantity lubrication–EMQL turning process. International Journal of Precision Engineering and Manufacturing-Green Technology, 2018, 5(2): 317–326
22. Lv T, Xu X F, Yu A B, Hu X D. Oil mist concentration and machining characteristics of SiO_2 water-based nano-lubricants in electrostatic minimum quantity lubrication-EMQL milling. Journal of Materials Processing Technology, 2021, 290: 116964
23. De Bartolomeis A, Newman S T, Shokrani A. High-speed milling inconel 718 using electrostatic minimum quantity lubrication (EMQL). Procedia CIRP, 2021, 101: 354–357
24. Xu J Y, Li L F, Lin T Y, Gupta M K, Chen M. Machinability analysis in high-speed milling of AlSi7Mg alloys under EMQL conditions: an approach toward sustainable manufacturing. Journal of Manufacturing Processes, 2022, 81: 1005–1017
25. Liu F C, Wu X Z, Xia Y, Lv T, Zhang R C, Hu X D, Xu X F. A novel cold air electrostatic minimum quantity lubrication (CAEMQL) technique for the machining of titanium alloys Ti–6Al–4V. The International Journal of Advanced Manufacturing Technology, 2023, 126(7–8): 3437–3452
26. Li L Y, Zhang Y B, Cui X, Said Z, Sharma S, Liu M Z, Gao T, Zhou Z M, Wang X M, Li C H. Mechanical behavior and modeling of grinding force: a comparative analysis. Journal of Manufacturing Processes, 2023, 102: 921–954
27. Liu D W, Li C H, Qin A G, Liu B, Chen Y, Zhang Y B. Kinematic analysis and milling force model of rotary surface milling machine of cutting machine. Journal of Mechanical Engineering, 2024, 1–13 (in Chinese)
28. Shi Z, Li C H, Liu D W, Zhang Y B, Qin A G, Cao H J, Chen Y. The instantaneous milling force model and verification of unequal helix angle end mill. Journal of Mechanical Engineering, 2024, 1–14 (in Chinese)

29. Zhou R H. Analytical model of milling forces prediction in five-axis milling process. The International Journal of Advanced Manufacturing Technology, 2020, 108(9): 3045–3054
30. He C L, Yan J W, Wang S Q, Zhang S, Chen G, Ren C Z. A theoretical and deep learning hybrid model for predicting surface roughness of diamond-turned polycrystalline materials. International Journal of Extreme Manufacturing, 2023, 5(3): 035102
31. Cui W Y, Chen H Z, Zhao J X, Ma Q S, Xu Q, Ma T B. Progresses on cryo-tribology lubrication mechanisms, detection methods and applications. International Journal of Extreme Manufacturing, 2023, 5(2): 022004
32. Chen N, Chen M J, Wu C Y, Pei X D, Qian J, Reynaerts D. Research in minimum undeformed chip thickness and size effect in micro end-milling of potassium dihydrogen phosphate crystal. International Journal of Mechanical Sciences, 2017, 134: 387–398
33. Mulyadi I H, Balogun V A, Mativenga P T. Environmental performance evaluation of different cutting environments when milling H13 tool steel. Journal of Cleaner Production, 2015, 108: 110–120
34. Duan Z J, Wang S S, Wang Z H, Li C H, Li Y H, Song J L, Liu J Y, Liu X. Tool wear mechanisms in cold plasma and nano-lubricant multi-energy field coupled micro-milling of Al–Li alloy. Tribology International, 2024, 192: 109337
35. Laghari R A, He N, Jamil M, Gupta M K. Tribological and machining characteristics of milling SiCp/Al MMC composites under sustainable cooling conditions. The International Journal of Advanced Manufacturing Technology, 2023, 128(5–6): 2613–2630
36. Sun J G, Li C H, Zhou Z M, Liu B, Zhang Y B, Yang M, Gao T, Liu M Z, Cui X, Li B K, Li R Z, Dambatta Y S, Sharma S. Material removal mechanism and force modeling in ultrasonic vibration-assisted micro-grinding biological bone. Chinese Journal of Mechanical Engineering, 2023, 36(1): 129
37. Su Y, Lu Q, Yu T, Liu Z Q, Zhang C Y. Machining and environmental effects of electrostatic atomization lubrication in milling operation. The International Journal of Advanced Manufacturing Technology, 2019, 104(5–8): 2773–2782
38. Zhang J Q, He B B, Zhang B. Failure mode change and material damage with varied machining speeds: a review. International Journal of Extreme Manufacturing, 2023, 5(2): 022003
39. Hu S G, Li C H, Zhou Z M, Liu B, Zhang Y B, Yang M, Li B K, Gao T, Liu M Z, Cui X, Wang X M, Xu W H, Dambatta Y S, Li R Z, Sharma S. Nanoparticle-enhanced coolants in machining: mechanism, application, and prospects. Frontiers of Mechanical Engineering, 2023, 18(4): 53
40. da Silva L R R, Ruzzi R S, Teles V C, Sales W F, Guesser W L, Machado A R. Analysis of the coefficient of friction at the workpiece–tool interface in milling of high strength compacted graphite cast irons. Wear, 2019, 426–427: 1646–1657
41. Zhao L, Zhang J J, Zhang J G, Dai H F, Hartmaier A, Sun T. Numerical simulation of materials-oriented ultra-precision diamond cutting: review and outlook. International Journal of Extreme Manufacturing, 2023, 5(2): 022001
42. Yang M, Kong M, Li C H, Long Y Z, Zhang Y B, Sharma S, Li R Z, Gao T, Liu M Z, Cui X, Wang X M, Ma X, Yang Y Y. Temperature field model in surface grinding: a comparative assessment. International Journal of Extreme Manufacturing, 2023, 5(4): 042011
43. Pham M Q, Yoon H S, Khare V, Ahn S H. Evaluation of ionic liquids as lubricants in micro milling–process capability and sustainability. Journal of Cleaner Production, 2014, 76: 167–173
44. Zhao G L, Xin L J, Li L, Zhang Y, He N, Hansen H N. Cutting force model and damage formation mechanism in milling of 70wt% Si/Al composite. Chinese Journal of Aeronautics, 2023, 36(7): 114–128
45. Dang J Q, Wang C G, Wang H H, An Q L, Wei J, Gao B, Liu Z M, Chen M. Deformation behavior and microstructure evolution of 300M ultrahigh strength steel subjected to high strain rate: an analytical approach. Journal of Materials Research and Technology, 2023, 25: 812–831
46. Sun C, Hong Y, Xiu S C, Ma L, Wang D W, Xu C W, Feng W. Surface strengthening mechanism of the active grinding carburization. Tribology International, 2023, 185: 108569
47. Wang X M, Li C H, Yang M, Zhang Y B, Liu M Z, Gao T, Cui X, Wang D Z, Cao H J, Chen Y, Liu B. Progress on the physical mechanism of microlubrication processing in nano bio-lubricants. Journal of Mechanical Engineering, 2024, 60(9): 286–322 (in Chinese)
48. Bai X F, Jiang J, Li C H, Dong L, Ali H M, Sharma S. Tribological performance of different concentrations of Al_2O_3 nanofluids on minimum quantity lubrication milling. Chinese Journal of Mechanical Engineering, 2023, 36(1): 11
49. Zhang J X, Zhang W, Li Z Y, Yan F Q, Liu Y H, Zhao Y G. Study on the influence of cutting parameters on specific cutting energy and surface roughness of radial tire mold side plate. Machine Tool and Hydraulic, 2021, 49(14): 36–40 (in Chinese)
50. Li C, Piao Y C, Zhang F H, Zhang Y, Hu Y X, Wang Y F. Understand anisotropy dependence of damage evolution and material removal during nanoscratch of MgF_2 single crystals. International Journal of Extreme Manufacturing, 2023, 5(1): 015101
51. Henke M, Lis B, Krystofiak T. Evaluation of surface roughness parameters of HDF for finishing under industrial conditions. Materials, 2022, 15(18): 6359
52. Dang J Q, Zhang H, An Q L, Ming W W, Chen M. On the microstructural evolution pattern of 300M steel subjected to surface cryogenic grinding treatment. Journal of Manufacturing Processes, 2021, 68: 169–185
53. Dang J Q, Zhang H, An Q L, Ming W W, Chen M. Surface modification of ultrahigh strength 300M steel under supercritical carbon dioxide ($scCO_2$)-assisted grinding process. Journal of Manufacturing Processes, 2021, 61: 1–14
54. Chen J, Yu W W, Zuo Z Y, Li Y G, Chen D, An Q L, Wang H W, Chen M. Tribological properties and tool wear in milling of *in-situ* TiB_2/7075 Al composite under various cryogenic MQL conditions. Tribology International, 2021, 160: 107021
55. An Q L, Cai C Y, Zou F, Liang X, Chen M. Tool wear and machined surface characteristics in side milling Ti6Al4V under dry and supercritical CO_2 with MQL conditions. Tribology International, 2020, 151: 106511
56. Pan Z R, Yao B, Chen B Q, Huang J S, Ma X F, Lan Q X. Cutting force model of milling titanium alloy with C60 nanofluid

minimum quantity lubrication. Journal of Manufacturing Processes, 2023, 105: 295–306

57. Yang M, Ma H, Hao J C, Li Z H, Li R Z, Zhou Z M, Gao T, Liu M Z, Cui X, Wang X M, Zhang Y B, Dambatta Y S, Long Y Z, Li C H. Droplet size distribution model of needle electrode electrostatic atomization and milling nickel-based alloy performance evaluation. Journal of Manufacturing Processes, 2024, 119: 682–698
58. Su Y, Wu S K, Jiang H. Study on the influence of base fluid type of external fluid on nanofluid coaxial electrostatic atomization cutting. China Mechanical Engineering, 2023, 34(7): 796–802 (in Chinese)
59. Su Y, Chu Z P, Gong L, Wang B, Liu Z Q. Assessment of lubrication property and machining performance of nanofluid composite electrostatic spraying (NCES) using different types of vegetable oils as base fluids of external fluid. Chinese Journal of Mechanical Engineering, 2023, 36(1): 94
60. Su Y, Hu X R, Zhang D D, Jiang H, Liu Z Q. Performance evaluation of composite electrostatic spraying (CES) in milling process. The International Journal of Advanced Manufacturing Technology, 2021, 117(1–2): 109–123
61. Liu D W, Xu Z L, Li C H, Qin A G, Liu B, Zhang Y B, Dambatta Y S, An Q L. Mathematical model and experimental verification of workpiece surface roughness in face milling. Surface Technology, 2024, 53(4): 125–139 (in Chinese)
62. Liu F, Shan Y Q, Gong Y D, Cai G Q. Cross correlation analysis on surface profile machined with abrasive jet precision finishing with grinding wheel as restraint. Diamond and Abrasive Engineering, 2007, 5: 53–57 (in Chinese)
63. Li X, Guan C M, Zhao P. Influences of milling and grinding on machined surface roughness and fatigue behavior of GH4169 superalloy workpieces. Chinese Journal of Aeronautics, 2018, 31(6): 1399–1405
64. Liu X H. Autocorrelation analysis of aluminum alloy grinding and processing surface. Light Alloy Fabrication Technology, 2010, 38(1): 41–42,59 (in Chinese)
65. Liu M Z, Li C H, Zhang Y B, Yang M, Gao T, Cui X, Wang X M, Li H N, Said Z, Li R Z, Sharma S. Analysis of grain tribology and improved grinding temperature model based on discrete heat source. Tribology International, 2023, 180: 108196
66. Wang J S, Fang F Z, An H J, Wu S, Qi H M, Cai Y X, Guo G Y. Laser machining fundamentals: micro, nano, atomic and close-to-atomic scales. International Journal of Extreme Manufacturing, 2023, 5(1): 012005
67. Kieren-Ehses S, Mayer T, Kirsch B, Aurich J C. Influence of the parameters of a minimum quantity lubrication system on micro milling process results. The International Journal of Advanced Manufacturing Technology, 2023, 127(11–12): 5279–5292
68. Huang W H, Yan J W. Effect of tool geometry on ultraprecision machining of soft-brittle materials: a comprehensive review. International Journal of Extreme Manufacturing, 2023, 5(1): 012003
69. Liang X L, Liu Z Q, Wang B, Wang C J, Cheung C F. Friction behaviors in the metal cutting process: state of the art and future perspectives. International Journal of Extreme Manufacturing, 2023, 5(1): 012002
70. Fulcheri L, Rohani V, Fabry F, Traisnel N. Experimental electrical characterization of a low-current tip–tip arc discharge in helium atmosphere at very high pressure. Plasma Sources Science & Technology, 2010, 19(4): 045010
71. Cai F F, Ren W, Chen X X. Optimization of high-speed milling parameters of integral impeller based on Taguchi method and variance analysis. Machine Tool and Hydraulics, 2016, 44(2): 4–6,9 (in Chinese)
72. Zhou Z, Li F, Yang H, Gao W Y, Miao L W. Orthogonal experimental study of soil–rock mixtures under the freeze–thaw cycle environment. International Journal of Pavement Engineering, 2021, 22(11): 1376–1388